



# Synergetic effect of carbon sphere derived from yeast with magnetism and cobalt oxide nanochains towards improving photodegradation activity for various pollutants

Xiaoxu Zhao<sup>a</sup>, Ziyang Lu<sup>a</sup>, Maobin Wei<sup>b</sup>, Menghan Zhang<sup>b</sup>, Hongjun Dong<sup>b,c</sup>, Chengwu Yi<sup>a,\*</sup>, Rong Ji<sup>b</sup>, Yongsheng Yan<sup>b,c,\*\*</sup>

<sup>a</sup> School of the Environment and Safety Engineering, Jiangsu University, Jiangsu, Zhenjiang 212013, PR China

<sup>b</sup> School of Chemistry and Chemical Engineering, Jiangsu University, Jiangsu, Zhenjiang 212013, PR China

<sup>c</sup> Institute of Green Chemistry and Chemical Technology, Jiangsu University, Jiangsu, Zhenjiang 212013, PR China



## ARTICLE INFO

### Keywords:

Yeast  
 $\text{Fe}_3\text{O}_4@\text{C}$   
 Cobalt oxides  
 Universal photocatalytic activity  
 Visible light

## ABSTRACT

Developing high-efficiency and low-cost semiconductor photocatalysts with carbon layer modification has been proved to possess the potential advantage for dramatically improved photocatalytic performance in recent years. Here, a novel magnetic core-shell  $\text{Fe}_3\text{O}_4@\text{C}$  modified with  $\text{Co}_3\text{O}_4$  nanochains photocatalyst ( $\text{Fe}_3\text{O}_4@\text{C}/\text{Co}_3\text{O}_4$ ) is first constructed via a facile synthetic strategy using inexpensive and ordinary yeast as carbon source. The obtained composite structure is conducive to the transfer and separation of charge carriers due to the synergetic effect of carbon layer and  $\text{Co}_3\text{O}_4$  nanochains. In consequence, the photodegradation activity of various pollutants is significantly enhanced relative to that of pure  $\text{Co}_3\text{O}_4$  under visible light irradiation. Moreover, the introduction of magnetic materials makes this photocatalyst recycled easily by an external magnetic field and reused effectively without obvious activity loss. This work may provide a feasibility analysis and exemplificative strategy for using simple raw materials as carbon source to observably improve universal photocatalytic activity of composite semiconductor photocatalyst.

## 1. Introduction

Over the past few years, water pollution is one of the most serious environmental problems, which becomes a formidable challenge to the sustainable development of modern human society. Semiconductor photocatalysis, as a kind of green technology, has achieved rapid development attributing to its potential advantages for solving the environmental pollution problem and energy crises [1–3]. As far as semiconductor photocatalysts are concerned, the photocatalytic activity of single semiconductor isn't very high generally. Thus, various modification strategies have been developed to further improve the photocatalytic performance, including doped with foreign elements [4–6], surface decoration with noble metal [7–9], constructed heterojunction with other energy-match semiconductor [10–13] and so on. Among those modified methods, carbon modified have attracted great attentions in recent years because of its unique superiorities contributing to the improvement of photocatalytic activity, such as the superior electrical conductivity, exceptional thermal properties, good light

absorption performance and so on. For example, Li et al. prepared carbon modified  $\text{Bi}_2\text{O}_3$  photocatalyst by one-step hydrolysis method using biochar as carbon source [14]. Core-shell structure  $\text{C}@\text{CdS}$  with a thin coating layer of amorphous carbon has also been prepared by one-pot hydrothermal carbonization method in the presence of glucose [15,16]. The improved photocatalytic activity of them confirmed that the introduced carbon material was an available modified way for semiconductor photocatalyst. Nevertheless, the carbon source they used always involves glucose, dimethylglyoxime, organic acid, maize cobs, etc., which may increase cost and complex preparation process as well as even cause secondary environment pollution. Therefore, it is necessary for exploiting a cost-effective, simple and eco-friendly carbon source to improve photocatalytic activity and other physicochemical property. Microorganism carbon may have a great foreground for this application due to its own advantages such as low cost, reproducible and abundant. It has been reported that the yeast carbon modified  $\text{TiO}_2$  not only has the biosorption ability of yeast but also improves the photocatalytic activity of  $\text{TiO}_2$  obviously [17–19]. Song et al. [20] also

\* Corresponding author at: School of the Environment and Safety Engineering, Jiangsu University, Jiangsu, Zhenjiang 212013, PR China.

\*\* Corresponding author at: School of Chemistry and Chemical Engineering, Jiangsu University, Jiangsu, Zhenjiang 212013, PR China. Institute of Green Chemistry and Chemical Technology, Jiangsu University, Jiangsu, Zhenjiang 212013, PR China.

E-mail addresses: [yichengwu0943@163.com](mailto:yichengwu0943@163.com) (C. Yi), [yys@mail.ujs.edu.cn](mailto:yys@mail.ujs.edu.cn) (Y. Yan).

obtained  $\text{TiO}_2$ -yeast carbon hybrid microspheres with controllable structures as photocatalyst. Those results demonstrated yeast can be an ideal choice as carbon source for photocatalyst modification. However,  $\text{TiO}_2$  can be only excited by the ultraviolet light due to its wide band gap (3.2 eV) and thus limits its practical application [21,22]. Therefore, designing and constructing of novel carbon modified visible-light semiconductor using yeast as carbon source is desired and significant to achieve high-performance photocatalysts.

As is well known, transition metal oxides have extensive application in the photocatalytic field due to the variety advantages of high stabilization, friendly environment, low cost and even visible-light photocatalytic activity [23,24]. Especially, cobalt oxide ( $\text{Co}_3\text{O}_4$ ) is a good candidate in photocatalytic field because of its interesting electronic structure, good light absorption performance and high thermal and chemical stability. However, pure  $\text{Co}_3\text{O}_4$  has a relatively low photocatalytic activity due to lower carrier separation efficiency [25]. Considering the above advantages of yeast as carbon source, we suspect if yeast was introduced into  $\text{Co}_3\text{O}_4$  system, it may be an effective way to improve its photocatalytic activity dramatically for practical application. Referring to the practical application of photocatalyst, it is very necessary to effectively separate and recycle the used photocatalyst to avoid secondary pollution and keep stability [26–28]. It is reported that core-shell structures with a magnetic core endue the materials with magnetic property and show superior separation effect [29,30]. Therefore, the incorporation of carbon and magnetic materials into the  $\text{Co}_3\text{O}_4$  system may be a very effective to greatly enhance photocatalytic activity and separate characteristics of  $\text{Co}_3\text{O}_4$ , which can further promote the value of practical application.

Herein, a novel carbon modified  $\text{Co}_3\text{O}_4$  nanochains photocatalyst ( $\text{Fe}_3\text{O}_4@\text{C}/\text{Co}_3\text{O}_4$ ) by using yeast as carbon source is successfully prepared by a facile and eco-friendly synthetic strategy for the first time. In comparison with the pure  $\text{Co}_3\text{O}_4$ , the  $\text{Fe}_3\text{O}_4@\text{C}/\text{Co}_3\text{O}_4$  exhibits superior universal photocatalytic degradation activity for various contaminants in the water under visible light, including antibiotic, heavy metal Cr(VI) and colored dye RhB. It derived from the synergistic effect of each function part in photocatalyst, in which the electrical conductivity of folium carbon facilitates electrons transfer from cobalt oxide. Additionally, the as-prepared photocatalysts could be easily separated from reaction solution by an external magnetic field. Therefore, this work extends the development of carbon source as carbon layer modification with other visible-light semiconductor photocatalyst to further improve universal photocatalytic activity and reusability for practical applications.

## 2. Experimental

### 2.1. Materials

The powdered yeast was purchased from Angel Yeast Company. Other reagents including ferric chloride hexahydrate ( $\text{FeCl}_3 \cdot 6\text{H}_2\text{O}$ ), ethylene glycol (EG), diethylene glycol (DEG), sodium acrylate ( $\text{CH}_2 = \text{CHCOONa}$ , Na acrylate), sodium acetate ( $\text{CH}_3\text{COONa}$ , NaOAc), citric acid, cetyltrimethylammonium bromide (CTAB), 1-hexanol, hexane, cobalt acetate, ammonium oxalate, chloroform, methanol, benzoquinone (BQ), isopropanol (IPA), triethanolamine (TEOA), 5,5-diamethyl-1-pyrroline N-oxide (DMPO) were obtained from Aladdin. Ethanol ( $\text{C}_2\text{H}_5\text{OH}$ , 95.0%) was purchased from Sinopharm Chemical Reagent Co.,Ltd. Tetracycline (TC), Cr (IV) and RhB dye were analytical pure and used without further purification, distilled water was used in the whole experiments.

### 2.2. Synthesis

#### 2.2.1. Synthesis of oxalate precursor

The synthesis of oxalate precursor is according to the reference [31]. Typically, microemulsions containing cetyltrimethylammonium bromide (CTAB, 2.0 g) as a surfactant, 1-hexanol (20 mL) as cosurfactant and hexane (35 mL) as the lipophilic phase were first prepared and were mixed separately with an aqueous solution of 0.1 M cobalt acetate and 0.1 M ammonium oxalate. Both microemulsions were mixed slowly and stirred overnight. The pink precipitate then obtained was centrifuged and washed with a 1/1 mixture of chloroform and methanol (200 mL) and subsequently dried at 60 °C for 12 h.

#### 2.2.2. Synthesis of magnetic core-shell $\text{Fe}_3\text{O}_4@\text{C}$

Yeast (0.1 ~ 0.5 g),  $\text{FeCl}_3 \cdot 6\text{H}_2\text{O}$  (2.4 g),  $\text{CH}_2 = \text{CHCOONa}$  (3.4 g), NaOAc (3.4 g) were added into a mixture of EG (22.5 mL) and DEG (22.5 mL) under ultrasonication for about 1 h. The homogeneous solution obtained was transferred to a Teflon-lined stainless-steel autoclave and sealed to heat at 200 °C. After reaction for 10 h, the autoclave was cooled to room temperature. The  $\text{Fe}_3\text{O}_4@\text{C}$  obtained was washed several times with ethanol and water, and then dried in vacuum at 65 °C for 10 h.

#### 2.2.3. Synthesis of magnetic core-shell $\text{Fe}_3\text{O}_4@\text{C}/\text{Co}_3\text{O}_4$ nanochains

$\text{Fe}_3\text{O}_4@\text{C}$  and cobalt oxalate precursor were added into EG under magnetic stirring for about 1 h. Then the samples with deionized water and ethanol washing several times and dried in vacuum at 65 °C for 10 h. Finally, the samples were heated to 400 °C at a rate of 2 °C/min in dry synthetic air (20%  $\text{O}_2$ , 80%  $\text{N}_2$ ) and kept at 400 °C for 8 h in a tubular furnace and then cooled to ambient temperature normally. The

**Scheme 1.** Schematic illustration of the preparation process of the  $\text{Fe}_3\text{O}_4@\text{C}/\text{Co}_3\text{O}_4$  sample.



preparation procedure of this photocatalyst is shown in Scheme 1.

### 2.3. Characterization

The scanning electron microscope (SEM) images and X-ray energy diffraction spectrum (EDS) were examined with JSM-7001F scanning electron microscopy (JEOL Ltd., Japan) while the transmission electron microscope (TEM) images were examined with JEM-2100 transmission electron microscopy (JEOL, Japan). The crystal phase was carried out by powder X-ray diffraction (XRD), which is obtained by X-ray diffractometer (MAC Science, Japan) equipped with Ni-filtrated Cu K $\alpha$  radiation (40 kV, 30 mA). The 2 $\theta$  scanning angle range was 5–80° at a scanning rate of 5° min<sup>-1</sup>. The optical properties of the samples were analyzed by UV-vis diffuse reflectance spectroscopy (DRS) with a specord 2450 spectrometer (Shimazu, Japan) in the wavelength range of 200–800 nm, in which BaSO<sub>4</sub> was used as the internal reflectance standard. Surface electronic states were analyzed on X-ray photoelectron spectroscopy (XPS, PerkinElmer PHI 5300). The specific surface area (BET) was estimated from the N<sub>2</sub> adsorption–desorption isotherms, measured by a Quantachrome NOVA4000 surface area apparatus. Magnetic measurement was carried out using a VSM (7300, Lakeshore) under a magnetic field up to 10 kOe. The photoluminescence (PL) spectra for solid samples were obtained on a F4500 (Hitachi, Japan) photoluminescence detector.

### 2.4. Adsorption experiments

For investigating the adsorption capability of photocatalysts, the adsorption experiments were as below. The photocatalyst was added into photocatalytic reactor containing various pollutants solutions with an injector in each 10 min after stirring for 60 min in the dark at 25 °C, the solutions were filtered and the concentration of various pollutants were determined with UV-vis spectroscopy, respectively.

### 2.5. Photocatalytic experiments

The photocatalytic activities were evaluated through decomposing various pollutants under visible light irradiation (a 300 W Xe lamp with a 420 nm cut off filter). The photocatalyst was totally suspended in an aqueous solution of TC (20 mg L<sup>-1</sup>), Cr (IV) (10 mg L<sup>-1</sup>) and RhB dye (10 mg L<sup>-1</sup>). Before irradiation, the suspensions were magnetically stirred in dark for 30 min to get absorption-desorption equilibrium between the photocatalyst and pollutants. At irradiation time interval of every 20 min (TC) was sampled and magnetic separated, then monitoring the absorbance. In addition, 0.02 g citric acid was added in the Cr (IV) solution before irradiation. Every 10 min of time intervals, 3 mL solution was collected from the suspension liquid, followed by centrifuged for 3 min. The absorbance of Cr (IV) solution determined using the diphenylcarbazide method and RhB solution was analyzed by measuring the absorbance through UV-vis spectrophotometer.

Moreover, the experiments of radicals capture were carried out by adding 1 mmol triethanolamine (TEOA, a quencher of h<sup>+</sup>), 1 mmol isopropanol (IPA, a quencher of ·OH), and 1 mmol benzoquinone (BQ, a quencher of ·O<sub>2</sub><sup>·-</sup>), respectively. The concentration of various pollutants in solution was determined by spectrophotometer. The photocatalytic efficiency was calculated according to Dr = (C<sub>0</sub>–C<sub>t</sub>)/C<sub>0</sub>, where Dr is the photocatalytic efficiency; C<sub>0</sub> is the concentration of reactant before illumination; C<sub>t</sub> is the concentration of reactant after illumination time.

### 2.6. Photoelectrochemical measurements

Incident-photon-to-current conversion efficiencies (IPCE) were calibrated with an electrochemical system (CHI 660B, Shanghai, China) using a standard three-electrode quartz cells with 0.5 M Na<sub>2</sub>SO<sub>4</sub> electrolyte solution, a Pt wire and a saturated calomel electrode (SCE) were

used as the counter electrode and the reference electrodes. Electrochemical impedance spectroscopy (EIS) was performed in a 0.5 M Na<sub>2</sub>SO<sub>4</sub> solution with a frequency range from 0.1 Hz to 100 kHz at 0.5 V. The amplitude of applied sine wave potential in each case was 5 mV which was carried out using a ZENNINIUM electrochemical workstation (Zahner Instruments, Germany), and all electrochemical signals were recorded by a CHI660 B electrochemical analyzer (Chen Hua Instruments, Shanghai, China). All electrodes were same as the electrodes using in IPCE.

### 2.7. Electron spin resonance (ESR) spectroscopy

ESR was introduced to characterize the formation of ·O<sub>2</sub><sup>·-</sup> and ·OH which were carried on a Brucker A300 ESR spectrometer at room temperature; ESR signals of spin-trapped paramagnetic species were verified with 5,5-diamethyl-1-pyrroline N-oxide (DMPO) [32]. The involvement of ·O<sub>2</sub><sup>·-</sup> was detected in methanol due to the instability of ·O<sub>2</sub><sup>·-</sup> in water, and the involvement of ·OH was examined in ultrapure water [33].

## 3. Results and discussion

The structural characterizations of the as-prepared Fe<sub>3</sub>O<sub>4</sub>, Fe<sub>3</sub>O<sub>4</sub>@C, Co<sub>3</sub>O<sub>4</sub> and Fe<sub>3</sub>O<sub>4</sub>@C/Co<sub>3</sub>O<sub>4</sub> samples are shown in Fig. 1. The similar diffraction characteristics in XRD patterns of Fe<sub>3</sub>O<sub>4</sub> and Fe<sub>3</sub>O<sub>4</sub>@C can be well-indexed as Fe<sub>3</sub>O<sub>4</sub> (JCPDS card No. 19-629), which implies the identical crystalline phase Fe<sub>3</sub>O<sub>4</sub> products are obtained and the carbon do not cause the phase change of Fe<sub>3</sub>O<sub>4</sub>. The absence of any crystalline phase of carbon in the XRD peaks implies that the carbon in the composite material is amorphous in nature [34–36]. The XRD peaks of Co<sub>3</sub>O<sub>4</sub> (JCPDS card No. 42-1467) crystal phase at 2θ = 19.0°, 31.2°, 36.5°, 44.8°, 59.0° and 65.2° are correspond to the reflection (111), (220), (311), (400), (511) and (440), respectively [37]. The sharp diffraction peaks and no other impurity phases indicate it has good purity and crystallinity. Furthermore, the diffraction peaks of the Fe<sub>3</sub>O<sub>4</sub>@C/Co<sub>3</sub>O<sub>4</sub> composite in each case correspond to the spinel lattice of Fe<sub>3</sub>O<sub>4</sub>, Fe<sub>3</sub>O<sub>4</sub>@C and Co<sub>3</sub>O<sub>4</sub> [38], the main diffraction peaks and their intensities have no obvious changes compared with that of the carbon, indicating the crystal structure in the composite samples keeps stable [3].

The morphology features of the as-prepared samples were investigated by SEM and TEM. As shown in Fig. 2(a and b), the SEM and TEM images of Co<sub>3</sub>O<sub>4</sub> exhibit nanochain structure and smooth surface. The microspheres are clearly loaded on Co<sub>3</sub>O<sub>4</sub> nanochains surface with

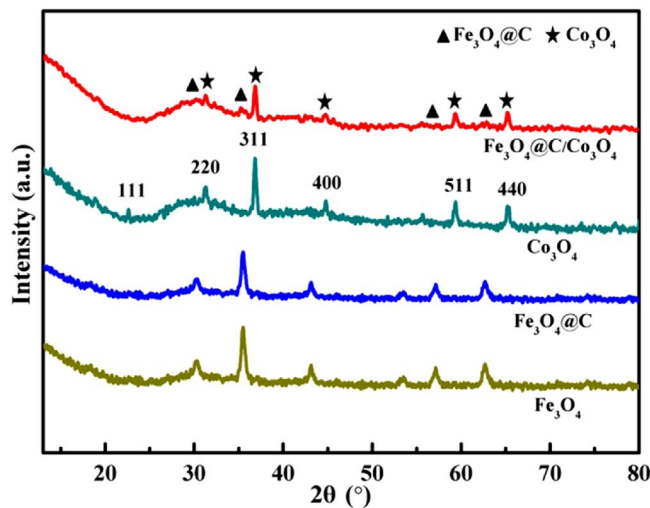
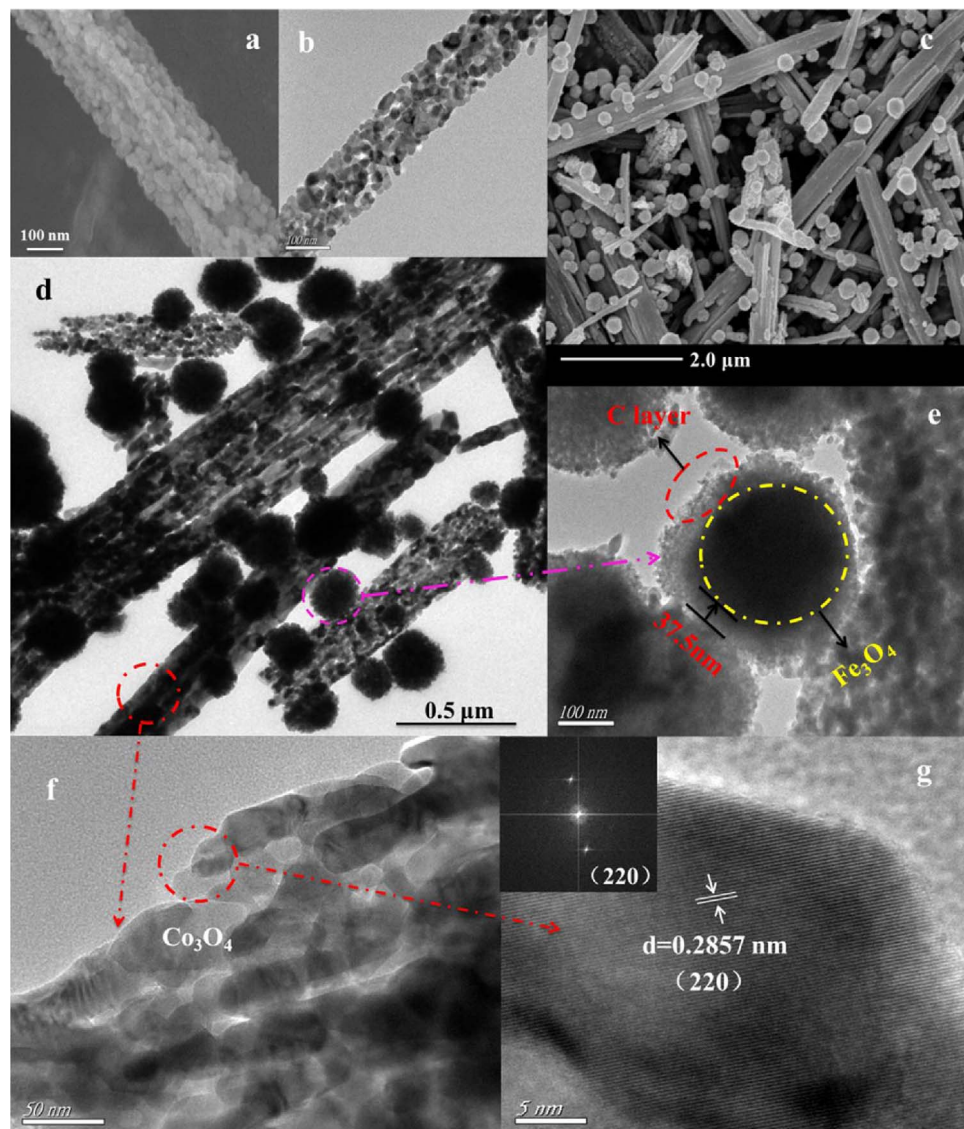


Fig. 1. XRD patterns of the as-prepared samples: Fe<sub>3</sub>O<sub>4</sub>@C/Co<sub>3</sub>O<sub>4</sub>, Co<sub>3</sub>O<sub>4</sub>, Fe<sub>3</sub>O<sub>4</sub> and Fe<sub>3</sub>O<sub>4</sub>@C.



**Fig. 2.** SEM images of  $\text{Co}_3\text{O}_4$  (a),  $\text{Fe}_3\text{O}_4@\text{C}/\text{Co}_3\text{O}_4$  (c), TEM image of  $\text{Co}_3\text{O}_4$  (b), HRTEM image (g) and FFT pattern (inset of g) of  $\text{Co}_3\text{O}_4$ , TEM image (d, e and f) of  $\text{Fe}_3\text{O}_4@\text{C}/\text{Co}_3\text{O}_4$ .

diameters of about 300 nm in Fig. 2c. Meanwhile, the TEM image in Fig. 2d proves those microspheres are core-shell structure ( $\text{Fe}_3\text{O}_4@\text{C}$ ). The thin carbon layer with the thickness of ~37.5 nm is also distinctly observed on the surface  $\text{Fe}_3\text{O}_4$  in Fig. 2e, which proved the formation of  $\text{Fe}_3\text{O}_4@\text{C}/\text{Co}_3\text{O}_4$  composite photocatalyst. It is noteworthy that the magnified TEM image of  $\text{Fe}_3\text{O}_4@\text{C}/\text{Co}_3\text{O}_4$  composite material presents a smooth surface in Fig. 2f. The interplanar spacing  $d$  value is 0.2857 nm from the HRTEM images (Fig. 2g), which corresponds to the (220) planes of monocrystal  $\text{Co}_3\text{O}_4$  sample. The corresponding fast Fourier transform (FFT) pattern of the crystallite in the inset of Fig. 2g further prove the above result. In addition, the elemental analysis results of this composite structure are shown in Table S1, it exhibits that the samples contain C, O, Co and Fe elements. All the results demonstrated the composite material of  $\text{Fe}_3\text{O}_4@\text{C}/\text{Co}_3\text{O}_4$  is prepared successfully with the yeast as carbon source.

It is well known that the optical absorption property of semiconductor plays an essential role in photocatalytic performance. The photophysical properties of the as-prepared photocatalysts were investigated by UV-vis diffuse reflectance spectroscopy. As shown in Fig. 3, the  $\text{Fe}_3\text{O}_4$  and  $\text{Fe}_3\text{O}_4@\text{C}$  samples present a wide and strong light absorption in the whole UV-vis range from 200 to 800 nm, demonstrating the thin C layer introducing has no obvious effect on photoabsorption of  $\text{Fe}_3\text{O}_4$ . Moreover, after combining with  $\text{Co}_3\text{O}_4$ , the light

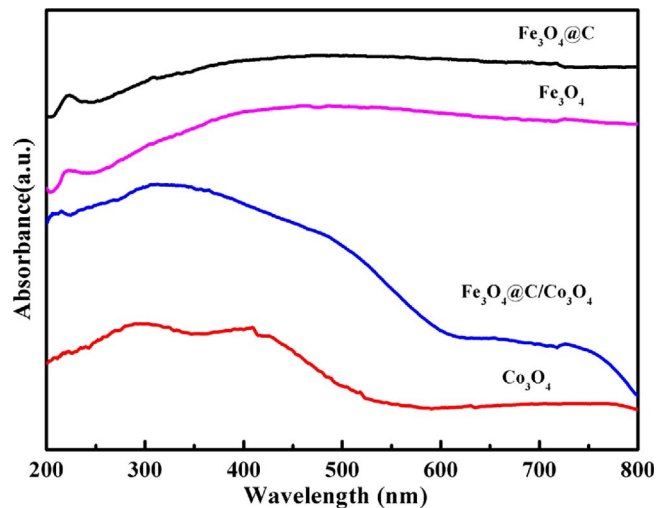


**Fig. 3.** UV-vis absorption spectra of  $\text{Fe}_3\text{O}_4@\text{C}/\text{Co}_3\text{O}_4$ ,  $\text{Co}_3\text{O}_4$ ,  $\text{Fe}_3\text{O}_4$  and  $\text{Fe}_3\text{O}_4@\text{C}$  samples.

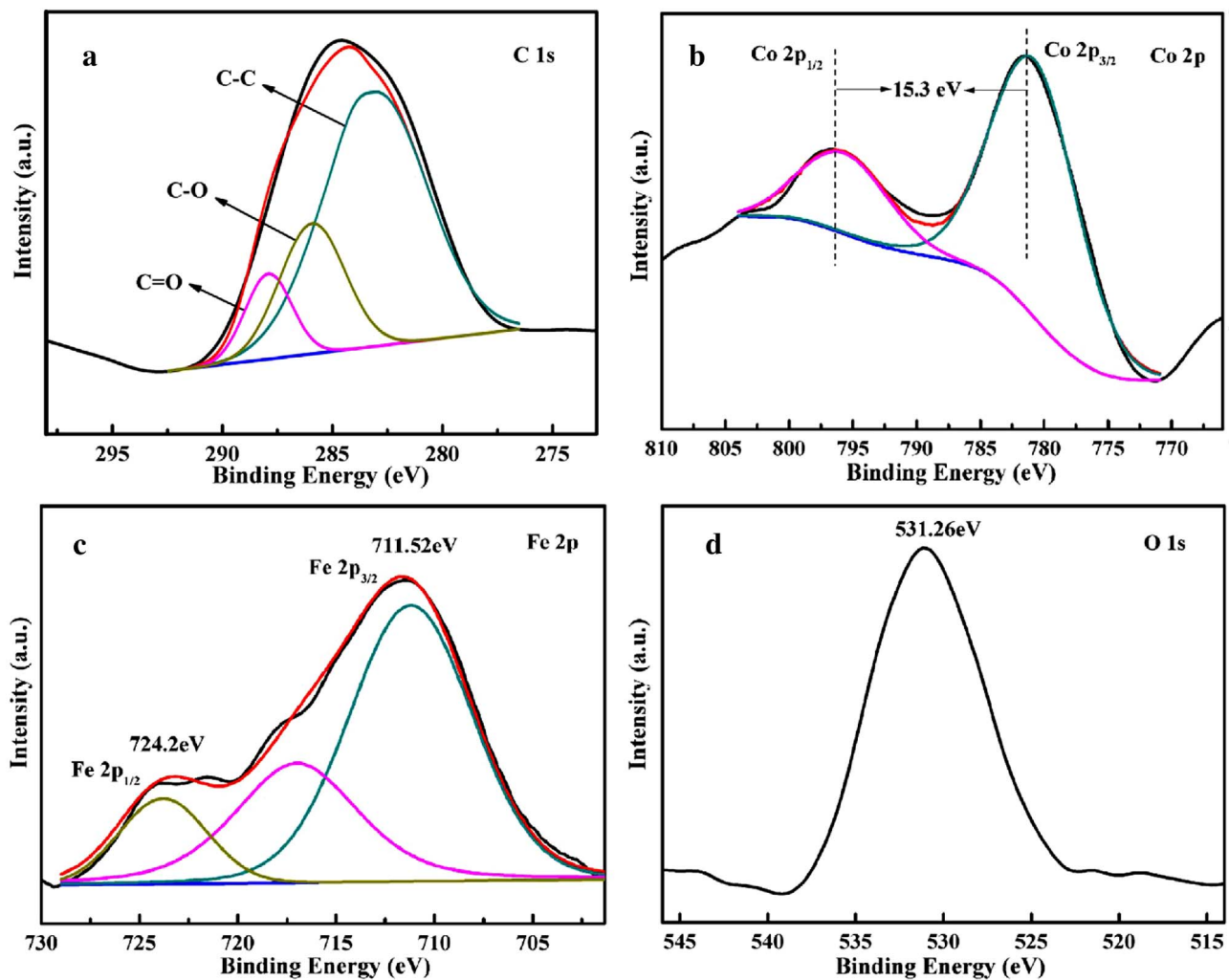


Fig. 4. XPS spectra of  $\text{Fe}_3\text{O}_4@\text{C}/\text{Co}_3\text{O}_4$  sample: C 1s (a), Co 2p (b), Fe 2p (c) and O 1s (d).

absorption ability of  $\text{Fe}_3\text{O}_4@\text{C}/\text{Co}_3\text{O}_4$  is significantly enhanced and its absorption edge has redshift compared with that of pure  $\text{Co}_3\text{O}_4$ . This result demonstrates the carbon material with magnetism widen the phototoabsorption range in visible light region of  $\text{Co}_3\text{O}_4$ , which is beneficial to improve photocatalytic activity. Furthermore, the BET surface area and pore diameter distribution are also an important influence factors on photocatalytic performance. The  $\text{N}_2$  adsorption-desorption isotherms of the prepared samples are listed in Table S2 (Supporting Information). Compared with the as-prepared  $\text{Co}_3\text{O}_4$  ( $35.57 \text{ m}^2 \text{ g}^{-1}$ ) and  $\text{Fe}_3\text{O}_4@\text{C}$  samples ( $6.43 \text{ m}^2 \text{ g}^{-1}$ ), the  $\text{Fe}_3\text{O}_4@\text{C}/\text{Co}_3\text{O}_4$  sample has the largest BET specific surface area values ( $42.85 \text{ m}^2 \text{ g}^{-1}$ ). It indicates that a larger surface area of  $\text{Fe}_3\text{O}_4@\text{C}/\text{Co}_3\text{O}_4$  sample is one of the important factors to improve its photocatalytic activity.

To obtain more information about the chemical composition and surface states of the composite structure, XPS analysis are conducted on  $\text{Fe}_3\text{O}_4@\text{C}/\text{Co}_3\text{O}_4$  sample. The XPS survey spectra (Fig. S2) shows the obvious binding energy peaks attribute to Co 2p, Co 3p, Fe 2p, Fe 3s, O 1s, C 1s state and O auger peaks, respectively. It demonstrates the as-prepared sample contained Co, Fe, C and O elements, which is well in line with the result of EDS spectrum (Fig. S1). As shown in Fig. 4a, the binding energy peak at 284.9 eV, 286.4 eV and 288.8 eV results from C 1 s state. The peaks at 284.9 eV and 286.4 eV are attributed to the carbon in C–C and C–O environments [39]. The peak at 288.8 eV could be assigned to the C=O from the oxalate anion [31]. The Co 2p<sub>1/2</sub> and Co 2p<sub>3/2</sub> binding energies in Fig. 4b are found to be at 796.2 eV and 780.9 eV, and the spin energy separation is 15.3 eV [40,41]. From the

XPS spectrum of Fe 2p (Fig. 4c), it exhibits two peaks at 711.52 and 724.2 eV, which should be assigned to Fe 2p<sub>3/2</sub> and Fe 2p<sub>1/2</sub>, respectively [42–44]. Moreover, as shown in Fig. 4d, the binding energy peak at 531.26 eV results from O 1 s state [3]. Those results further demonstrate the  $\text{Fe}_3\text{O}_4@\text{C}/\text{Co}_3\text{O}_4$  sample was obtained, which is also in accordance with the XRD analysis.

Antibiotics, as one of the most common pharmaceuticals, are found in the aquatic environment in recent years. It is considered as the serious environmental pollution problems owing to their antimicrobial nature. Therefore, we first investigate the photocatalytic activity of the as-prepared samples through the photodegradation experiments for common antibiotics under visible light. As shown in Fig. 5a, the solution system of TC reached the adsorption-desorption balance within 30 min. It is obvious that the adsorption capacity of  $\text{Fe}_3\text{O}_4@\text{C}/\text{Co}_3\text{O}_4$  is much higher than that of  $\text{Fe}_3\text{O}_4@\text{C}$ ,  $\text{Fe}_3\text{O}_4/\text{Co}_3\text{O}_4$  and  $\text{Co}_3\text{O}_4$ . Additionally, Fig. 5b displayed the absorbance variation curves of TC solutions over  $\text{Fe}_3\text{O}_4@\text{C}/\text{Co}_3\text{O}_4$  during degradation reaction process, in which the absorption peaks of TC at ultraviolet and visible region are disappearing gradually, indirectly proving that the TC molecules are decomposed into the small molecules or ions [45]. The dynamic curves of photodegradation TC over the as-prepared samples are shown in Fig. 5c, it exhibits that the photocatalytic activity for degradation TC are negligible over  $\text{Fe}_3\text{O}_4@\text{C}$  and no photocatalyst. However, the photocatalytic activities over  $\text{Fe}_3\text{O}_4@\text{C}/\text{Co}_3\text{O}_4$  sample are obvious higher than that of pure  $\text{Co}_3\text{O}_4$  and  $\text{Fe}_3\text{O}_4/\text{Co}_3\text{O}_4$ . Furthermore, the kinetic curves of TC photodegradation can be approximated as a pseudo-first-

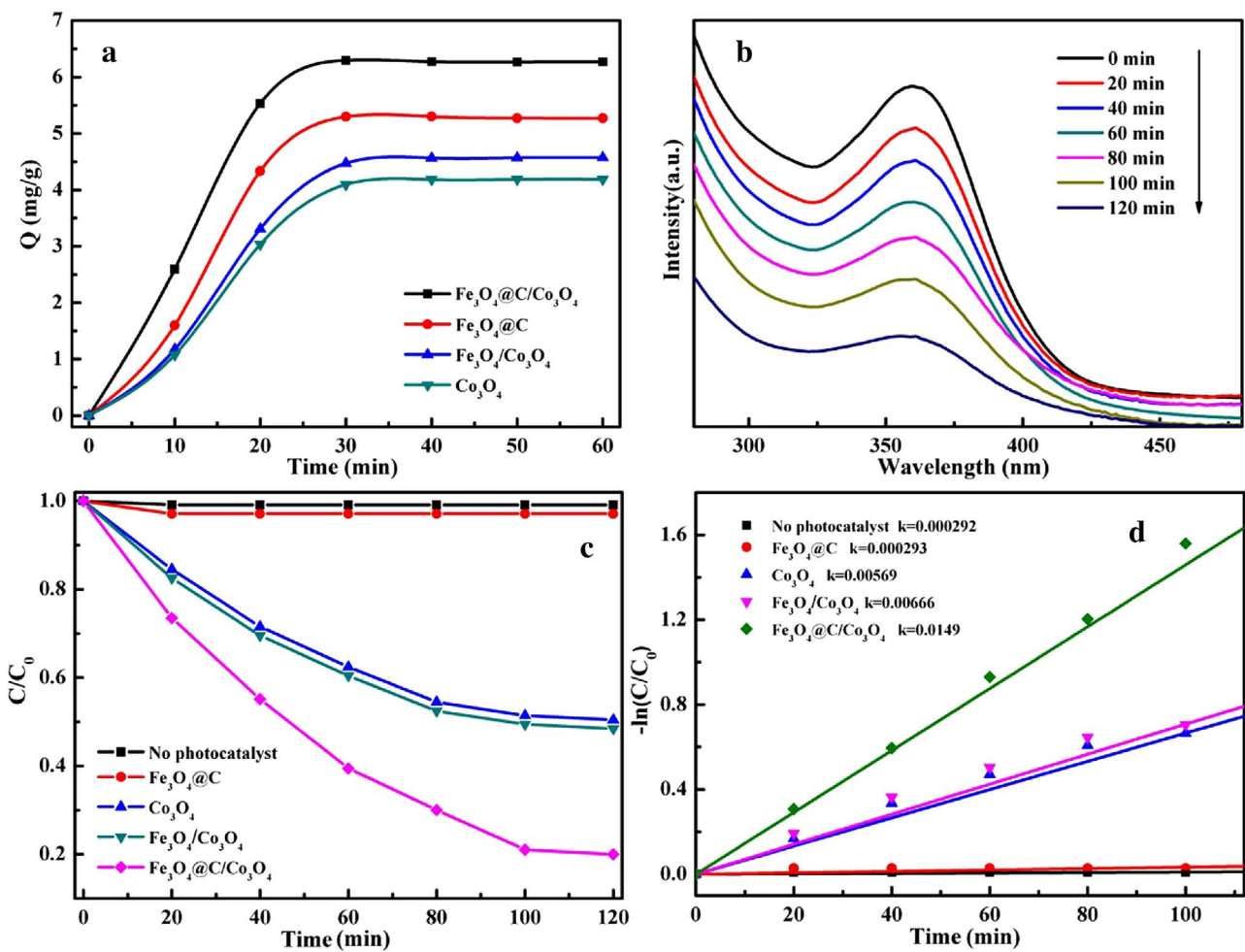


Fig. 5. The TC absorption curves (a), absorption spectra variations (b), dynamic curves of photodegradation TC (c) and plots of  $-\ln(C/C_0)$  versus time (d) over different samples.

order process and the plots of  $-\ln(C/C_0)$  versus time are performed (Fig. 5d). The removal rate constant  $k$  of TC photodegradation over  $\text{Fe}_3\text{O}_4@\text{C}/\text{Co}_3\text{O}_4$  is  $0.0149 \text{ min}^{-1}$ , which reaches to 2.62, 2.24 and 51 times as much as that of  $\text{Co}_3\text{O}_4$  ( $0.00569 \text{ min}^{-1}$ ),  $\text{Fe}_3\text{O}_4/\text{Co}_3\text{O}_4$  ( $0.00666 \text{ min}^{-1}$ ) and no photocatalyst ( $0.00029 \text{ min}^{-1}$ ), respectively.

As we all know, the reusability and stability of the photocatalysts

are also crucial factors for practical application. We investigate the photodegradation stability of  $\text{Fe}_3\text{O}_4@\text{C}/\text{Co}_3\text{O}_4$  sample through degradation of TC. As can be seen from Fig. 6a, the degradation of pollutants activity of  $\text{Fe}_3\text{O}_4@\text{C}/\text{Co}_3\text{O}_4$  shows hardly any loss after five cycles reuse. In addition, the XRD pattern (Fig. S4) also illustrated that the structure of the  $\text{Fe}_3\text{O}_4@\text{C}/\text{Co}_3\text{O}_4$  photocatalysts did not change

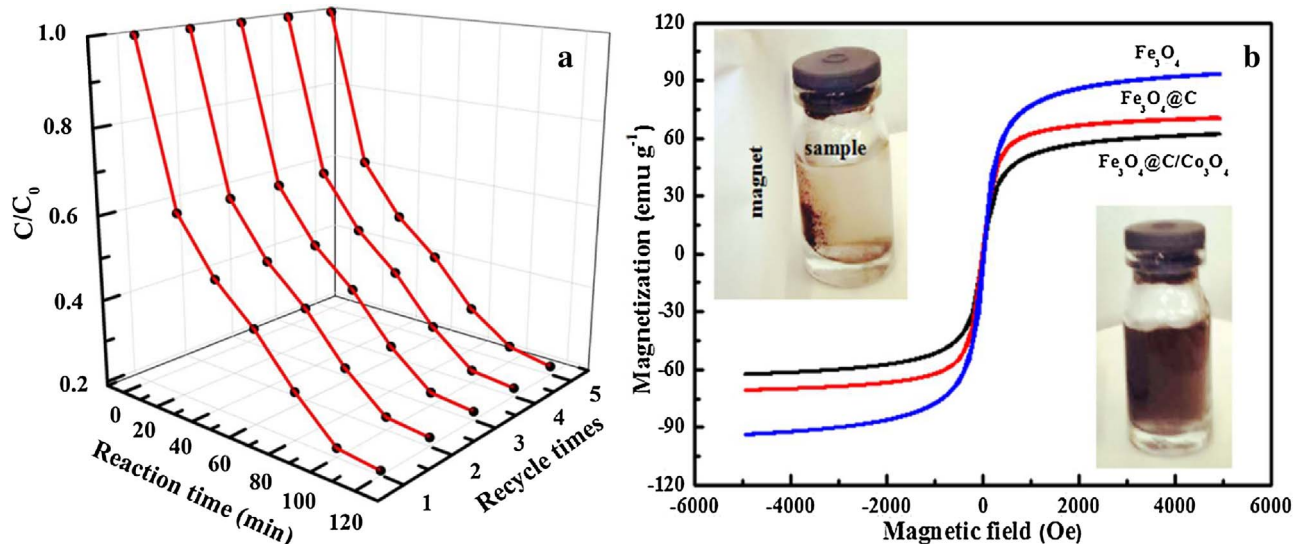


Fig. 6. Cycle runs (a), hysteresis loops recorded at 300 K (inset: separation of  $\text{Fe}_3\text{O}_4@\text{C}/\text{Co}_3\text{O}_4$  from solution under an external magnetic field) (b) over different samples.

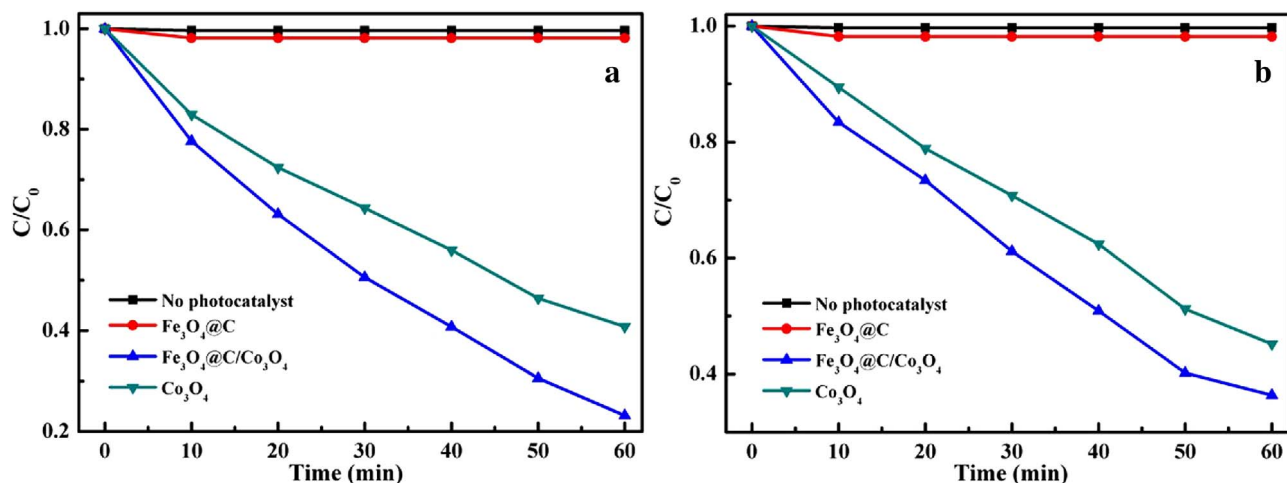


Fig. 7. Dynamic curves of Cr(VI) photoreduction (a) and RhB solution (b) over different samples.

after the photocatalytic reaction. The above results confirm that Fe<sub>3</sub>O<sub>4</sub>@C/Co<sub>3</sub>O<sub>4</sub> sample is a stable and durable photocatalyst. Furthermore, in order to evaluate the magnetic behavior of the nanocomposites, the magnetic measurements were carried out at 300 K. The magnetization saturation values (Ms) of the Fe<sub>3</sub>O<sub>4</sub>, Fe<sub>3</sub>O<sub>4</sub>@C and Fe<sub>3</sub>O<sub>4</sub>@C/Co<sub>3</sub>O<sub>4</sub> (Fig. 6b) were measured to be 93.6, 70.8 and 62.3 emu g<sup>-1</sup>, respectively. The magnetic separability of Fe<sub>3</sub>O<sub>4</sub>@C/Co<sub>3</sub>O<sub>4</sub> was tested in water by placing a magnet near the glass bottle (the inset of Fig. 6b). The photocatalysts are attracted toward the magnet within few seconds, which demonstrates the Fe<sub>3</sub>O<sub>4</sub>@C/Co<sub>3</sub>O<sub>4</sub> sample has excellent magnetic properties.

It is widely known that Cr(VI) contamination in natural water has harmful effects on human health. Green photocatalysis technology is recognized as a promising way for reducing Cr(VI) to the less toxic Cr (III) due to its unique advantage [46,47]. So we further investigate the photocatalytic activity of as-prepared samples through photoreduction of Cr(VI). As can be observed from Fig. 7a, the Fe<sub>3</sub>O<sub>4</sub>@C/Co<sub>3</sub>O<sub>4</sub> sample shows the highest photocatalytic activity for reducing Cr(VI) in the all of as-prepared samples in the presence of citric acid which served as the sacrificial agent for capturing photogenerated holes because of its electron rich property to improve the separation efficiency of charge carriers. Besides heavy metal solution, the colored dyes are also common industrial organic pollutants [48]. In the work, the typical RhB dye is selected as representative to discuss the pervasive photocatalytic activity of the as-prepared samples. Fig. 7b shows the degradation dynamic curves for the colored RhB dye, Fe<sub>3</sub>O<sub>4</sub>@C/Co<sub>3</sub>O<sub>4</sub> presents the much higher photocatalytic degradation ability than that of Co<sub>3</sub>O<sub>4</sub> in the same way. However, the photocatalytic activities of Fe<sub>3</sub>O<sub>4</sub>@C are also insignificant. All of the above results demonstrate that the introduction of carbon materials using ordinary yeast as carbon source expand the photocatalytic function of Co<sub>3</sub>O<sub>4</sub>, which may become the promising strategy for practical application of photodecomposing diversified contaminants in water.

The photocatalytic mechanism exploration experiment was carried out to investigate the main active species during photocatalytic degradation process via dissolving different trapping agents in solution. As can be seen from Fig. 8a for the representative TC photodegradation under visible light, when the TEOA and BQ are added into reaction solution, the photocatalytic activity are reduced. It indicates that hole (h<sup>+</sup>) and superoxide radical (·O<sub>2</sub><sup>-</sup>) are the main activated species. However, the degradation rate for TC slightly decreased upon the addition of the IPA. It implies that hydroxyl radicals (·OH) has also slightly effect on the photodegradation TC. The influence order of the photodegradation process for TC is h<sup>+</sup> > ·O<sub>2</sub><sup>-</sup> > ·OH. In addition, in order to further explore the photodegradation TC reaction mechanism over Fe<sub>3</sub>O<sub>4</sub>@C/Co<sub>3</sub>O<sub>4</sub> sample, the ESR technique is carried out

to detect the active species during the photodegradation TC process over Fe<sub>3</sub>O<sub>4</sub>@C/Co<sub>3</sub>O<sub>4</sub> sample under visible light. As seen in Fig. 8b, four characteristic peaks of DMPO → ·O<sub>2</sub><sup>-</sup> species are observed in methanol dispersion of Fe<sub>3</sub>O<sub>4</sub>@C/Co<sub>3</sub>O<sub>4</sub> sample under visible light irradiation. Meanwhile, the weak characteristic peaks of DMPO → ·OH species are detected in Fe<sub>3</sub>O<sub>4</sub>@C/Co<sub>3</sub>O<sub>4</sub> aqueous dispersions under visible light irradiation (Fig. 8c). The above results demonstrate that ·O<sub>2</sub><sup>-</sup>, ·OH and photogenerated holes are the main active species during the photocatalytic process.

As is known that mass spectrometry is used to detect the photocatalytic intermediate products, the possible intermediate products of photodegradation of TC were tested in this experiment. The results are shown in Fig. 9, the prominent anion with m/z of 445 is the deprotonated TC molecular ion [49,50], during the process of degradation, the TC is fragmented into small molecules (Fig. 10): m/z = 445 → m/z = 406 (by loss of OH, H and CH<sub>3</sub>) → m/z = 362 (by loss of CONH<sub>2</sub>) → m/z = 318 (by loss of N, CH<sub>2</sub> and CH<sub>3</sub>) → m/z = 274 (then by loss of CH, C, H and OH). Finally, with the change of time, the TC is gradually broken down into small molecules.

The photocatalytic activity is closely concerned with the electron transport behavior. The intense photocurrent suggests the high charge collection efficiency on the electrode surface, and indirectly evidences the high separated efficiency of electron-hole pairs [51,52]. The Fe<sub>3</sub>O<sub>4</sub>@C/Co<sub>3</sub>O<sub>4</sub> electrode exhibits the greater photocurrent response than that of Co<sub>3</sub>O<sub>4</sub> electrode under visible light (Fig. 11a), which demonstrates that the former can separate electron-hole pairs more effectively. In addition, electrochemical impedance spectroscopy (EIS) is another valid electrochemical strategy to account for the electron-transfer efficiency on the electrodes [53]. In general, a higher mobility and separation of photoexcited electron-hole pairs result in a smaller EIS arc radius [53]. From Fig. 11b, Fe<sub>3</sub>O<sub>4</sub>@C/Co<sub>3</sub>O<sub>4</sub> is smaller radius than that of Co<sub>3</sub>O<sub>4</sub>, demonstrating that a fast interfacial charge transfer property in the Fe<sub>3</sub>O<sub>4</sub>@C/Co<sub>3</sub>O<sub>4</sub> sample. Additionally, it is reported that photoluminescence (PL) emission is mainly caused by the recombination of electron-hole pairs [54]. Fig. S5 shows that the PL emission peaks of two samples locate at 337 nm, which ascribes to the transfer of band gap. The lower PL intensity of Fe<sub>3</sub>O<sub>4</sub>@C/Co<sub>3</sub>O<sub>4</sub> sample indicates the recombination of charge carriers is greatly inhibited. The photoelectrochemical and photoluminescent characteristics reveal enhancing the transfer and separation efficiency of electrons-hole pairs is the main reason for improving the Fe<sub>3</sub>O<sub>4</sub>@C/Co<sub>3</sub>O<sub>4</sub> universal photocatalytic activity.

In order to further investigate the photocatalytic mechanism, the potential of the photocatalyst valence band and conduction band was determined by UV-vis DRS spectra and valence band spectra (Fig. S6). The E<sub>g</sub> of Co<sub>3</sub>O<sub>4</sub> in Fe<sub>3</sub>O<sub>4</sub>@C/Co<sub>3</sub>O<sub>4</sub> calculated by a plot of ( $\alpha h\nu$ )<sup>2</sup>

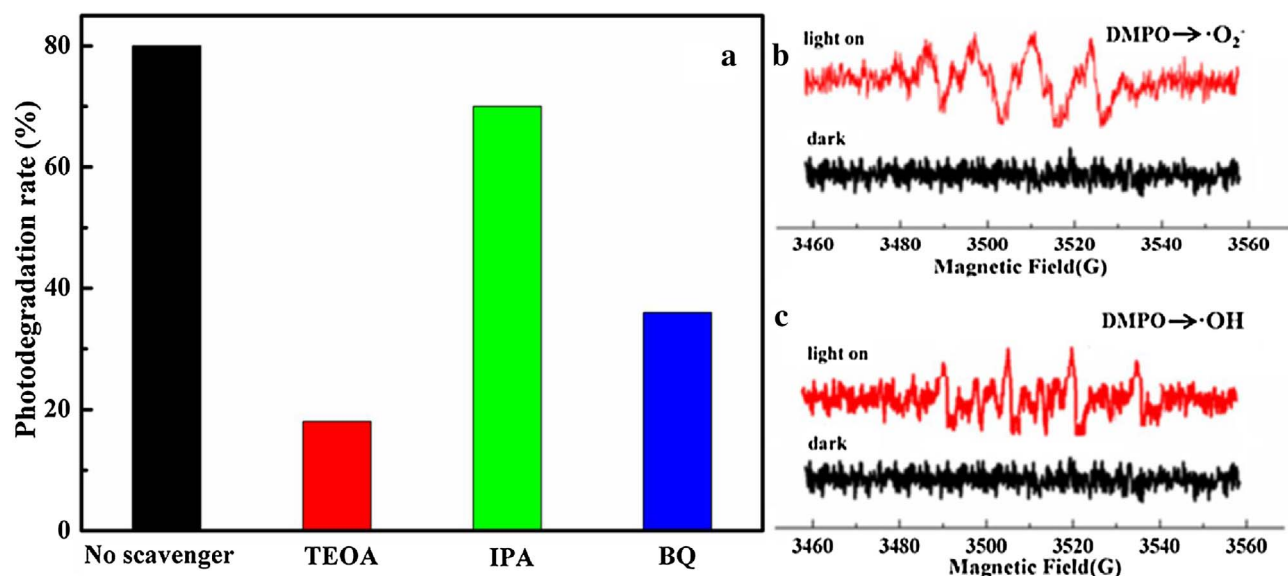


Fig. 8. Trapping experiments of the active species during the photocatalytic degradation of pollutants in the presence of the  $\text{Fe}_3\text{O}_4@\text{C}/\text{Co}_3\text{O}_4$  (a); DMPO spin-trapping ESR spectra with  $\text{Fe}_3\text{O}_4@\text{C}/\text{Co}_3\text{O}_4$  in the dark and under visible light irradiation at ambient temperature (b, c).

versus  $(h\nu)$  was about 1.98 eV and the measured  $E_{VB}$  was about 1.50 eV. Thus, the  $E_{CB}$  of  $\text{Fe}_3\text{O}_4@\text{C}/\text{Co}_3\text{O}_4$  was about  $-0.48$  eV. Therefore, on the basis of the above experimental results and theory analyses, a possible photocatalytic reaction mechanism for  $\text{Fe}_3\text{O}_4@\text{C}/\text{Co}_3\text{O}_4$  is proposed schematically in Scheme 2. When the  $\text{Fe}_3\text{O}_4@\text{C}/\text{Co}_3\text{O}_4$  sample serves as photocatalyst, the electrons-hole pairs generate under visible light irradiation, then separate and transfer to the sample surface. The phototo-generated electrons ( $e^-$ ) of  $\text{Co}_3\text{O}_4$  may transfer to C

layer due to its unique electrical conductivity, which may be captured by the dissolved oxygen in water to produce superoxide radicals ( $\cdot\text{O}_2^-$ ). Meanwhile, a little part of  $\cdot\text{O}_2^-$  may also react with  $\text{H}^+$  to further produce  $\cdot\text{OH}$ . The generated  $\cdot\text{O}_2^-$ ,  $\cdot\text{OH}$  and holes all directly oxidize the pollutants adsorbed on the surface. It should point out that, in this photoreaction process, the universal photocatalytic activity of the  $\text{Fe}_3\text{O}_4@\text{C}/\text{Co}_3\text{O}_4$  photocatalyst was hardly affected by  $\text{Fe}_3\text{O}_4$ , but it is the key that  $\text{Fe}_3\text{O}_4$  as magnetic material not only enable magnetic

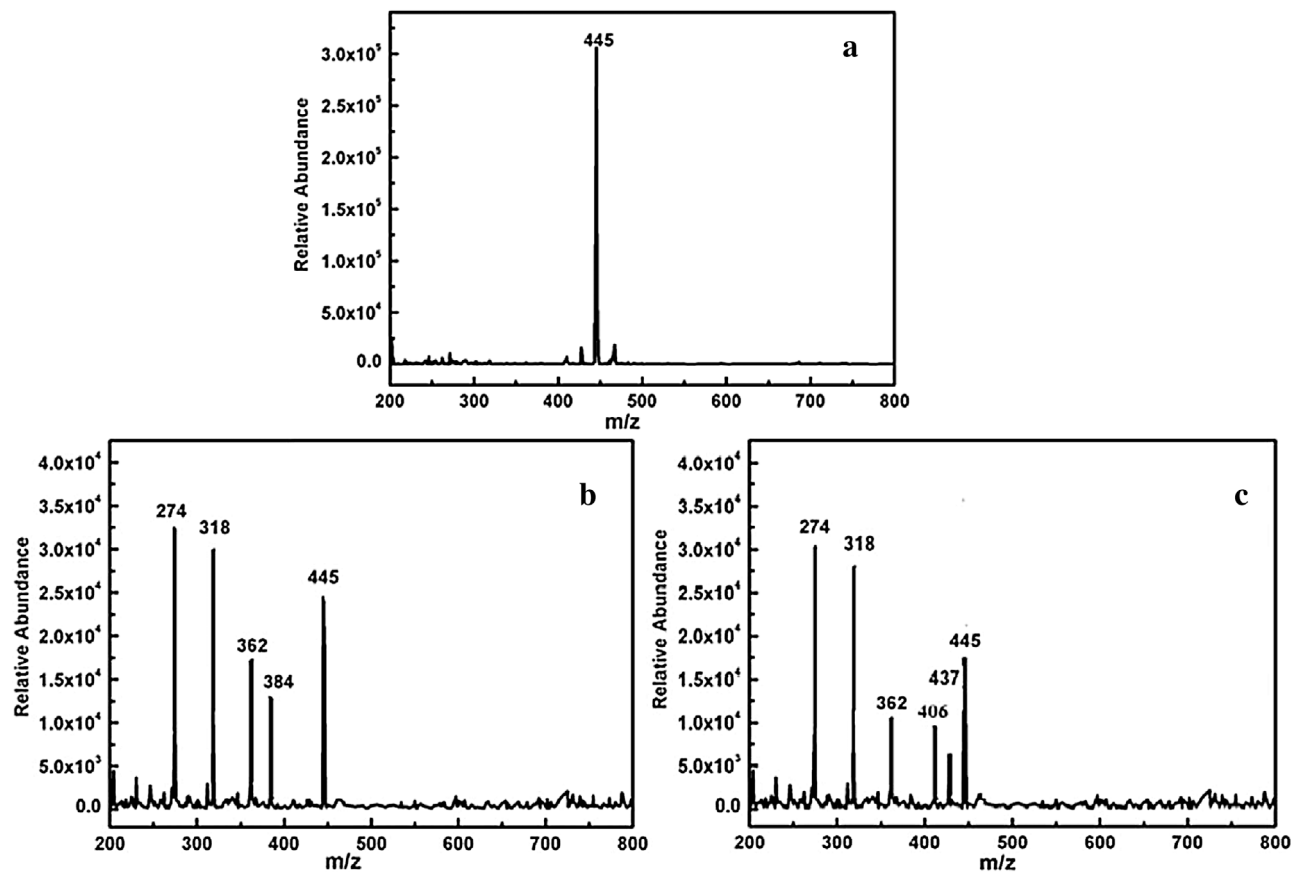


Fig. 9.  $m/z$  of degrading TC over  $\text{Fe}_3\text{O}_4@\text{C}/\text{Co}_3\text{O}_4$  composite photocatalyst: the initial tetracycline solution (a); degradation of TC after 60 min (b); degradation of TC after 120 min (c).

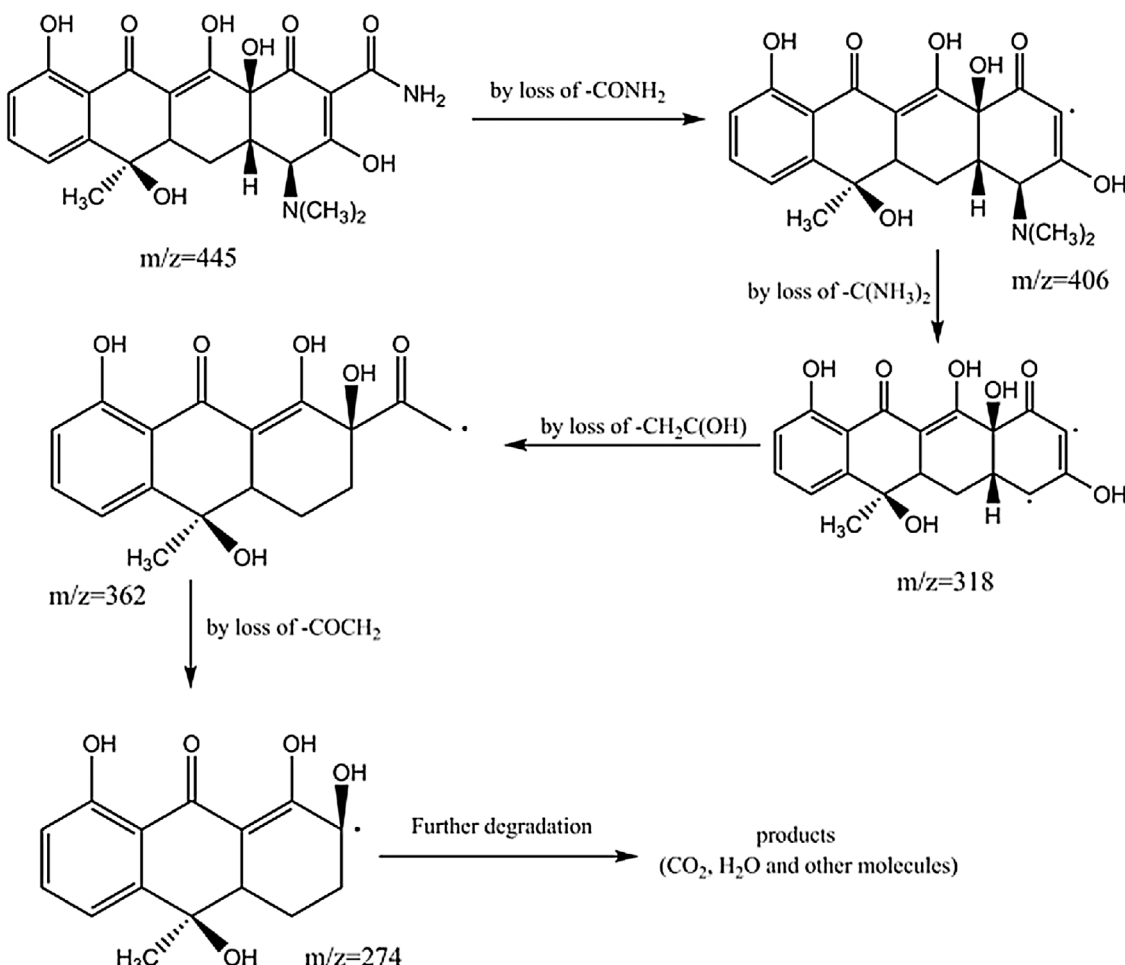


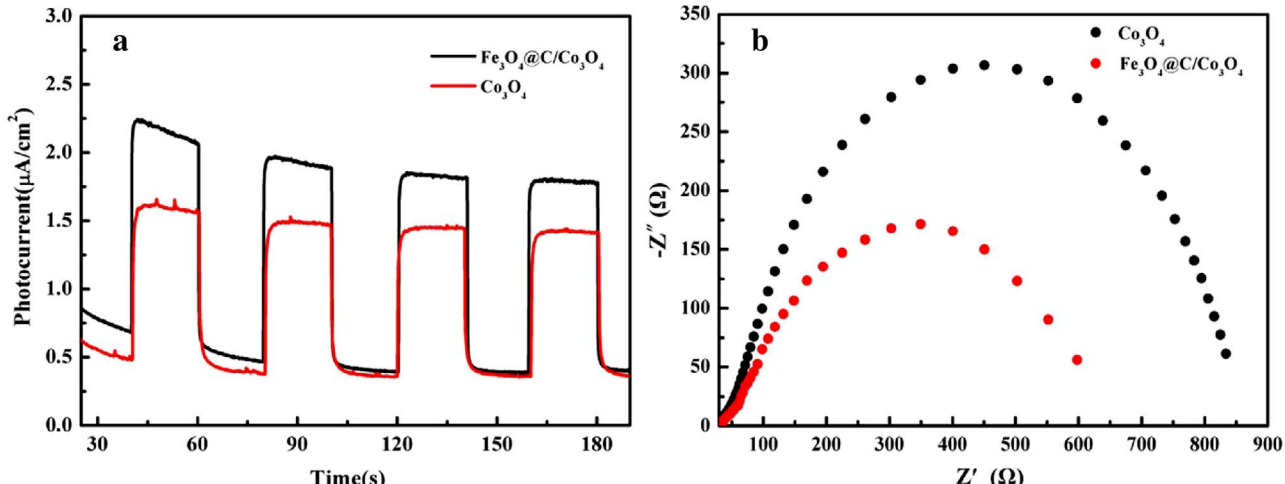
Fig. 10. The steps of degradation TC during the photoreaction process under visible light.

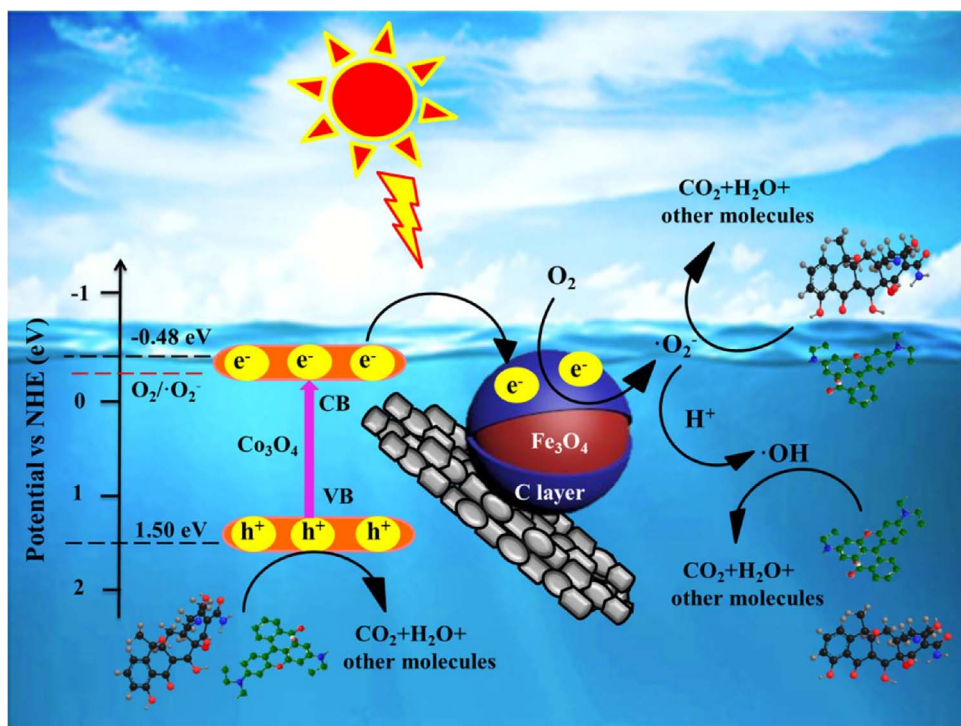
separation but also facilitate the catalysts to be recycled.

#### 4. Conclusions

In summary, a multifunctional and highly efficient carbon modified  $\text{Co}_3\text{O}_4$  nanochains photocatalyst ( $\text{Fe}_3\text{O}_4@\text{C}/\text{Co}_3\text{O}_4$ ) by using yeast as carbon precursor is firstly prepared via a simple method. The

$\text{Fe}_3\text{O}_4@\text{C}/\text{Co}_3\text{O}_4$  sample shows the higher photocatalytic activity than that of pure  $\text{Co}_3\text{O}_4$  for the degradation various pollutants under visible light irradiation, including antibiotic, Cr(VI) and RhB dye. The enhanced universal photocatalytic degradation activity of the  $\text{Fe}_3\text{O}_4@\text{C}/\text{Co}_3\text{O}_4$  sample is due to the introduction of the carbon material facilitating transfer and separation of charge carriers. Furthermore, the high magnetic performance of the as-prepared  $\text{Fe}_3\text{O}_4@\text{C}/\text{Co}_3\text{O}_4$  samples is

Fig. 11. Transient photocurrent response of  $\text{Co}_3\text{O}_4$  and  $\text{Fe}_3\text{O}_4@\text{C}/\text{Co}_3\text{O}_4$  nanocomposites under visible-light irradiation (a); Nyquist plots of the EIS data of the  $\text{Co}_3\text{O}_4$  and  $\text{Fe}_3\text{O}_4@\text{C}/\text{Co}_3\text{O}_4$  (b).



**Scheme 2.** Possible photocatalytic reacation me-  
chanism for degradation contaminants over the  
 $\text{Fe}_3\text{O}_4@\text{C}/\text{Co}_3\text{O}_4$  photocatalyst under visible light.

favorable for the separation and recycling from the reaction media after the photocatalytic reactions. Therefore, the composite photocatalyst shows the outstanding photostability and recyclability. This work not only develops a promising carbon source of yeast but also gives a new direction to design other composite semiconductor photocatalyst for broadening the universal photocatalytic activity for environmental remediation.

## Acknowledgements

This work was financially supported by the National Natural Science Foundation of China (Nos. 21407059, 21407064 and 21606114), the Natural Science Foundation of Jiangsu Province (Nos. BK20140527, BK20140532 and BK20150536), the Postdoctoral Science Foundation of Jiangsu Province (No. 15011102B).

## Appendix A. Supplementary data

Supplementary data associated with this article can be found, in the online version, at <http://dx.doi.org/10.1016/j.apcatb.2017.08.037>.

## References

- [1] A. Fujishima, Nature 238 (1972) 37–38.  
[2] C. Chen, W. Ma, J. Zhao, Chem. Soc. Rev. 39 (2010) 4206–4219.  
[3] C. Tang, E. Liu, J. Wan, X. Hu, J. Fan, Appl. Catal. B: Environ. 181 (2016) 707–715.  
[4] A. Mukherji, R. Marschall, A. Tanksale, C. Sun, S.C. Smith, Q.L. Gao, L. Wang, Adv. Funct. Mater. 21 (2011) 125.  
[5] J. Fu, B. Zhu, C. Jiang, B. Cheng, W. You, J. Yu, Small 13 (2017) 1603938.  
[6] A. Phuruangrat, P. Dumrongrojathanath, S. Thongtem, T. Thongtem, Mater. Lett. (2017) 114–117.  
[7] B. Tian, C. Li, F. Gu, H. Jiang, Catal. Commun. 10 (2009) 925–929.  
[8] S. Ghasemi, S.J. Hashemian, A.A. Alamolhoda, I. Gocheva, S.R. Setayesh, Mater. Res. Bull. 87 (2017) 40–47.  
[9] T. Li, G. Lu, X. Hu, W. Xie, Q. Xia, S. Luo, Mater. Lett. 188 (2017) 392–395.  
[10] X. Ma, Z. Ma, T. Liao, X. Liu, Y. Zhang, L.L. Li, W. Li, B. Hou, J. Alloy. Compd. 702 (2017) 68–74.  
[11] H. Liu, D. Chen, Z. Wang, H. Jing, R. Zhang, Appl. Catal. B: Environ. 203 (2016) 300–313.  
[12] J. Wang, L. Tang, G. Zeng, Y. Deng, Y. Liu, L. Wang, Y. Zhou, Z. Guo, J. Wang, C. Zhang, Appl. Catal. B: Environ. 209 (2017) 285–294.  
[13] J. Zhao, J. Nan, Z. Zhao, N. Li, J. Liu, F. Cui, Appl. Catal. B: Environ. 202 (2017) 509–517.  
[14] M. Li, H. Huang, S. Yu, N. Tian, F. Dong, X. Du, Y. Zhang, Appl. Surf. Sci. 386 (2016) 285–295.  
[15] Y. Hu, X. Gao, L. Yu, Y. Wang, J. Ning, S. Xu, X.W. Lou, Angew. Chem. 52 (2013) 5636–5639.  
[16] J. Chen, F. Zhang, Y.L. Zhao, Y.C. Guo, P. Gong, Z.Q. Li, H.S. Qian, Appl. Surf. Sci. 362 (2015) 126–131.  
[17] B. Bai, L. Chen, J. Cao, Y. Li, Chem. Eng. 40 (2012) 64–69.  
[18] B. Bai, N. Quici, Z. Li, G.L. Puma, Chem. Eng. J. 170 (2011) 451–456.  
[19] L. Chen, B. Bai, Equilibrium, Kinetic, Ind. Eng. Chem. Res. 52 (2013) 15568–15577.  
[20] R. Song, B. Bai, D. Jing, J. Chem. Technol. Biotechnol. 90 (2014) 930–938.  
[21] S. Verbruggen, M. Keulemans, M. Filippousi, D. Flahaut, G. Van Tendeloo, S. Lacombe, J. Martens, S. Lenaerts, Appl. Catal. B: Environ. 156 (2014) 116–121.  
[22] H. Yaghoubi, Z. Li, Y. Chen, H.T. Ngo, V.R. Bhethanabotla, B. Joseph, S. Ma, R. Schlaf, A. Takshi, ACS Catal. 5 (2014) 327–325.  
[23] M.C. Scharber, Adv. Mater. 28 (2016) 1994–2001.  
[24] L. Pan, L. Li, D. Tian, C. Li, J. Wang, JOM 66 (2014) 1035–1042.  
[25] Y. Zheng, W. Wang, D. Jiang, L. Zhang, Chem. Eng. J. 284 (2015) 21–27.  
[26] W.H. Li, X.P. Yue, C.S. Guo, J.P. Lv, S.S. Liu, Y. Zhang, J. Xu, Appl. Surf. Sci. 335 (2015) 23–28.  
[27] K. Chen, G.H. Wang, W.B. Li, D. Wan, Q. Hu, L.L. Lu, Chin. Chem. Lett. 25 (2014) 1455–1460.  
[28] Y.F. Zhang, L.G. Qiu, Y.P. Yuan, Y.J. Zhu, X. Jiang, J.D. Xiao, Appl. Catal. B: Environ. 144 (2014) 863–869.  
[29] L. Zhang, S.Z. Qiao, Y.G. Jin, Z.G. Chen, H.C. Gu, G.Q. Lu, Adv. Mater. 20 (2008) 805–809.  
[30] T. Yao, T. Cui, J. Wu, Q. Chen, X. Yin, F. Cui, K. Sun, Carbon 50 (2012) 2287–2295.  
[31] P.W. Menezes, A. Indra, D. González-Flores, N.R. Sahraie, I. Zaharieva, M. Schwarze, P. Strasser, H. Dau, M. Driess, ACS Catal. 5 (2015) 2017–2027.  
[32] M.J. Zhou, J.Z. Li, Z.F. Ye, C.C. Ma, H.Q. Wang, P.W. Huo, W.D. Shi, Y.S. Yan, ACS Appl. Mater. Interfaces 7 (2015) 28231–28243.  
[33] W. Wang, T.W. Ng, W.K. Ho, J. Huang, S. Liang, T. An, G. Li, J.C. Yu, P.K. Wong, Appl. Catal. B: Environ. 129 (2013) 482–490.  
[34] A. Banerjee, R. Gokhale, S. Bhatnagar, J. Jog, M. Bhardwaj, B. Lefez, B. Hannoyer, S. Ogale, J. Mater. Chem. 22 (2012) 19694–19699.  
[35] Y. Guo, H. Wang, C. He, L. Qiu, X. Cao, Langmuir 25 (2009) 4678–4684.  
[36] Y. Hu, X. Gao, L. Yu, Y. Wang, J. Ning, S. Xu, X.W.D. Lou, Angew. Chem. 125 (2013) 5746–5749.  
[37] T. Warang, N. Patel, R. Fernandes, N. Bazzanella, A. Miotello, Appl. Catal. B: Environ. 132 (2013) 204–211.  
[38] A. Banerjee, R. Gokhale, S. Bhatnagar, J. Jog, M. Bhardwaj, B. Lefez, B. Hannoyer, S. Ogale, J. Mater. Chem. 22 (2012) 19694–19699.  
[39] L. Wang, K. Gan, D. Lu, J. Zhang, Eur. J. Inorg. Chem. 2016 (2016) 890–896.  
[40] G. Chen, X. Si, J. Yu, H. Bai, X. Zhang, Appl. Surf. Sci. 330 (2015) 191–199.  
[41] G.L. Chen, C. Guyon, Z.X. Zhang, S. Ognier, J. Beem, M. Tatoulian, Mater. Lett. 107 (2013) 111–114.  
[42] Z. Xing, Z. Ju, J. Yang, H. Xu, Y. Qian, Nano Res. 5 (2012) 477–485.  
[43] J. Luo, J. Liu, Z. Zeng, F.N. Chi, L. Ma, H. Zhang, J. Lin, Z. Shen, H.J. Fan, Nano Lett. 13 (2013) 6136–6143.  
[44] T. Xia, X. Xu, J. Wang, C. Xu, F. Meng, Z. Shi, J. Lian, J.M. Bassat, Electrochim. Acta

- 160 (2015) 114–122.
- [45] H. Dong, G. Chen, J. Sun, C. Li, Y. Yu, D. Chen, *Appl. Catal. B: Environ.* 134 (2013) 46–54.
- [46] Y. Yang, G. Wang, Q. Deng, D.H.L. Ng, H. Zhao, *ACS Appl. Mater. Interfaces* 6 (2014) 3008–3015.
- [47] L. Yang, W. Sun, S. Luo, Y. Luo, *Appl. Catal. B: Environ.* 156 (2014) 25–34.
- [48] L. Yang, Y. Xiao, S. Liu, Y. Li, Q. Cai, *Appl. Catal. B: Environ.* 94 (2010) 142–149.
- [49] X.L. Liu, P. Lv, G.X. Yao, C.C. Ma, P.W. Huo, Y.S. Yan, *Chem. Eng. J.* 217 (2013) 398–406.
- [50] N.L. Gao, Z.Y. Lu, X.X. Zhao, Z. Zhu, Y.S. Wang, D.D. Wang, Z.F. Hua, C.X. Li, P.W. Huo, M.S. Song, *Chem. Eng. J.* 304 (2016) 351–361.
- [51] H.J. Dong, G. Chen, J.X. Sun, Y.J. Feng, C.M. Li, G.H. Xiong, C.D. Lv, *Dalton Trans.* 43 (2014) 72–82.
- [52] C.M. Li, G. Chen, J.X. Sun, Y.J. Feng, J.J. Liu, H.J. Dong, *Appl. Catal. B: Environ.* 163 (2015) 415–423.
- [53] C.M. Li, G. Chen, J.X. Sun, J.C. Rao, Z.H. Han, Y.D. Hu, W.N. Xing, C.M. Zhang, *Appl. Catal. B: Environ.* 188 (2016) 39–47.
- [54] H. Zhang, R. Zong, Y. Zhu, *J. Phys. Chem. C* 113 (2009) 4605–4611.